Supplementary Materials for

Chaos-assisted broadband momentum transformation in optical microresonators

Xuefeng Jiang,* Linbo Shao,* Shu-Xin Zhang, Xu Yi, Jan Wiersig, Li Wang, Qihuang Gong, Marko Lončar, Lan Yang, Yun-Feng Xiao†

*These authors contributed equally to this work.
†Corresponding author. Email: yfxiao@pku.edu.cn

Published 20 October 2017, *Science* **358**, 344 (2017)
DOI: 10.1126/science.aao0763

This PDF file includes:

Materials and Methods
Supplementary Text
Figs. S1 to S13
Caption for Movie S1
References

Other Supporting Online Material for this manuscript includes the following:
(available at www.sciencemag.org/content/358/6361/344/suppl/DC1)

Movie S1

Materials and Methods

Device fabrication

The deformed microtoroids are fabricated from a 2-μm-thickness silicon dioxide layer on a silicon wafer. The consecutive fabrication procedures for microtoroids are following: (i) photolithography defining device patterns, (ii) buffered hydrofluoric acid etch transferring the device patterns to the oxide layer, (iii) XeF_2 gas silicon etch suspending rims of the devices, (iv) pulsed CO_2 laser reflowing the suspended rims forming microtoroids, and (v) XeF_2 gas etch shrinking the silicon supports of silicon dioxide cavity (*33*).

The tapered fiber waveguides are fabricated from a commercial single-mode optical fiber. The fiber is tapered by pulling using a stepper motor, while it is being heated over an oxyhydrogen flame. This pulling process is programmed to fabricate various tapered fibers with desired sizes.

Experimental measurement

The experimental setup consists of following components. (i) Tunable external-cavity lasers serve as the probe/pump light. The laser polarization if adjusted by a fiber polarization controller. (ii) A tapered fiber waveguide is used for coupling to microresonators. (iii) A three-axis nano-translation stage (Thorlabs, MDT630A, with 20 nm resolution) is utilized to optimize the coupling positions between the microresonators and the tapered fiber waveguide. (iv) A microresonator is placed on the translation stage. For the deformed resonators, the fiber waveguide is placed at position $\phi = \pi/2$ or $3\pi/2$ in deformed cavity coordinate, referring to **Fig. S6A**. The incident light is propagating towards 0 degree in cavity coordinate. (v) Photoreceivers (Newport, 1801-FC, 320 nm - 1,000 nm, and 1811-FC, 900 nm - 1,700 nm) and an oscilloscope (YOKOGAWA, DLM2034) are used to measure and capture the transmission intensity of the fiber waveguide (**Fig. 3** in the main text). (vi) Two optical spectrum analyzers (OSAs) (OSA-1: YOKOGAWA, AQ6319, 600 nm - 1,700 nm, with 0.02 nm resolution; OSA-2: Ocean Optics, HR4000, 200 nm - 1,100 nm, with 0.27 nm resolution) are used in the third-harmonic generation experiment (**Fig. 4** in the main text).

3D FDTD numerical simulations

The three-dimensional (3D) numerical simulations are performed by a commercial-grade simulator (*34*) based on the finite-difference time-domain (FDTD) method. The 3D FDTD simulation region is sized 36 μm, 38 μm, and 16 μm in *x*, *y*, and *z* axes, with perfectly matched layer (PML) absorbing boundary conditions at each limit. The microtoroid resonator is sitting on the *x*-*y* plane, the principal and minor diameters of the microtoroid are 24 μm and 4 μm, and the thickness of the central disk is 2 μm. The waveguide in the simulation is represented by a cylinder with a diameter of 0.5 μm. The probe light source, which is a short pulse with a duration of 10 fs, is applied to one end of the waveguide. The symmetry about the *x*-*y* plane is used to reduce the computational expense. Short time electromagnetic (EM) fields at whispering gallery mode (WGM) resonant frequency are obtained by frequency domain monitors with a time apodization of 350 fs, as shown in **Fig. S1**.

Calculation of mode index and WGM proportion

The mode index and the WGM proportion shown in **Fig. 2F** in the main text are extracted from the short time frequency domain monitors in 3D FDTD simulation. The mode index n_{mode} is calculated as following,

$$n_{mode} = \sqrt{\frac{\int E(x,y,z)\,\epsilon(x,y,z)\,E^{*}(x,y,z)\,dxdydz}{\int E(x,y,z)E^{*}(x,y,z)\,dxdydz}}, \tag{S1}$$

where $E(x,y,z)$ and $\varepsilon(x,y,z)$ are the electrical field and the permittivity of the material at position (x, y, z), respectively.

The WGM proportion $\eta_{\mathrm{WGM}}(t)$ at time t is calculated by projecting the electrical field $E(t;x,y,z)$ to the field of the established WGM $E_{\mathrm{WGM}}(x,y,z)$. In the simulation, the $E_{\mathrm{WGM}}(x,y,z)$ is the stabilized field after 200 ps simulation time. The expression of $\eta_{\mathrm{WGM}}(t)$ is given by,

$$\eta_{WGM}(t) = \left| \frac{\int E(t;x,y,z)E^{*}_{\mathrm{WGM}}(x,y,z)\,dxdydz}{\sqrt{\int |E(t;x,y,z)|^{2}\,dxdydz \cdot \int |E_{\mathrm{WGM}}(x,y,z)|^{2}\,dxdydz}} \right|. \tag{S2}$$

The increase of the mode index in **Fig. 2F** indicates that the light is being coupled into the cavity, and the momentum of light is moving towards the WGM. The comparably slow increase of the WGM proportion reveals the dynamic tunneling between the chaotic fields and the high-Q WGM.

Temporal dynamics of coupling

We model the dynamic tunneling between the chaotic fields and the WGM to a two-level system by reducing the continuum of chaos to a single state. In this case, the transition between the chaotic fields and the WGM is treated incoherently (*35*). The equation of motion for the photon counts is given by,

$$\begin{aligned} \dot{n}_{\mathrm{m}} &= -\gamma_m n_m + \kappa\left(n_c - n_m\right), \\ \dot{n}_c &= -\gamma_c n_c + \kappa\left(n_m - n_c\right), \end{aligned} \tag{S3}$$

where n_{m} and n_{c} are photon numbers in the WGM and the chaotic fields; γ_m and γ_c are optical decay rates of the WGM and the chaotic fields, respectively; κ is the effective tunneling rate between the two states. Giving the boundary condition that light initial resides in chaos, i.e., $n_m = 0, n_c = 1$, the WGM proportion η is analytically solved as

$$\eta(t) = \frac{n_m}{n_c + n_m} = \frac{2\kappa}{\gamma_m - \gamma_c + 2\kappa + \sqrt{\left(\gamma_c - \gamma_m\right)^2 + 4\kappa^2}\,\coth\left[\frac{1}{2}t\sqrt{\left(\gamma_c - \gamma_m\right)^2 + 4\kappa^2}\right]}. \tag{S4}$$

This is well fitted with the simulation results in **Fig. 2F** in the main text. Additionally, the maximum slope of the WGM proportion η is given by

$$\dot{\eta}(t)\big|_{\max} = \frac{1}{4}\left(\gamma_c - \gamma_m\right) + \frac{\kappa^2}{\gamma_c - \gamma_m} \tag{S5}$$

when $\gamma_c - \gamma_m > 2\kappa$, which is fulfilled by the leaky chaotic modes.

Supplementary Text

I. Additional experimental data

A. Broadband Raman laser experiment

To demonstrate the broadband excitation property and the role of the sub-wavelength nanowaveguide in the chaos-assisted momentum-transformation-enabled coupling mechanism, we excite the deformed microtoroidal resonator *simultaneously* in the 780 nm and 1,550 nm wavelength bands using three different-sized fibers, as shown in **Fig. S2**. For the fiber with diameter d~1.71 μm (0.98 μm) satisfying phase-matching conditions in the 1,550 nm (770 nm) wavelength band, first-order Raman lasers are observed in only one wavelength band (*36*). For example, the optical fiber of d~1.71 μm couples efficiently to the cavity modes in the 1,550 nm wavelength band and produces first-order Raman laser (no higher order cascade Raman laser is observed due to the limitation of the band of the OSA-1 (600 nm - 1,700 nm)); while the coupling is too weak to give rise to observable signal of stimulated Raman scattering in the 770 nm wavelength band (**Fig. S2A**). On the contrary, the optical fiber of d~0.98 μm generates cascaded Raman lasers (*37*) in the 770 nm wavelength band but fails in the 1,550 nm band (**Fig. S2B**). Remarkably, by using a sub-wavelength fiber of d~0.46 μm, the (cascaded) Raman lasers in both wavelength bands are observed simultaneously, because the momentum-transformation enables the broadband coupling (**Fig. S2C**).

B. Experimental results of THG versus waveguide diameters

To further demonstrate the role of the nanowaveguide in the chaos-assisted momentum-transformed mechanism, we excite the deformed microtoroidal resonator and collect the same THG emission using a tapered fiber waveguide with different diameters, as shown in **Fig. S3**. The THG conversion efficiency of the device is obtained by the collected THG signal in OSA-2 divided by the cubed input power, $P_{\mathrm{THG}} / P_{\mathrm{in}}^3$. This definition of nonlinear efficiency is independent on P_{in}. The conversion efficiency enhancement factor is normalized to the highest conversion efficiency of direct phase-matched coupling using micro-sized tapered fiber waveguide (i.e., the reference point marked by the red arrow in **Fig. S3**). The experimental results conclude that the momentum-transformed scheme enhances the conversion efficiency of the device by over three orders than the direct phase-matched coupling. Positions for the tapered fiber and the cavity are optimized to maximize the THG signal for each data point.

C. Stability of momentum-transformation-enabled coupling

For real photonics applications, stability is crucial for photonic devices (*38-41*). Time stability of coupling (*42*) is studied by using two tapered fibers with diameters of 0.46 μm and 1.71 μm, as shown in **Fig. S4**. The measurement of the 0.46-μm fiber is performed by directly contacting the fiber waveguide with the resonator boundary, which shows an excellent linewidth stability with an uncertainty of 0.5 MHz over one hour. While for the 1.71-μm fiber, an appropriate fiber-cavity gap is chosen to couple to the same WGM with a high coupling efficiency. The measured linewidth of 1.71-μm fiber coupling increases significantly over time.

In addition, we measure the loaded Q factors from transmission spectra by simply contacting the tapered fibers of different diameters to the equatorial plane of the toroid. Typical transmission spectra using different sized fibers are shown in **Fig. S5A**, where loaded Q factors are obtained. As shown in **Fig. S5B**, when the diameter is smaller than 0.8 μm, the loaded Q factors of the WGM in the 1,550 nm wavelength band remain almost unchanged and close to the intrinsic Q factor. While the diameter is larger than 0.8 μm, the loaded Q factor generally decreases with increasing diameter due to the increasing coupling loss, which corresponds to the transferring from the momentum-transformed coupling to direct phase-matched coupling.

II. Design of resonator and waveguide

A. Ray dynamics analysis of deformed microresonator

The deformed toroidal microcavities, supporting ultrahigh-Q WGMs, which can be effectively excited by the chaos-assisted momentum-transformed coupling method, have the boundaries defined in the polar coordinates as (*33, 43*)

$$R(\phi)=\begin{cases} R_0+R_0\sum_{i=2,3} a_i\cos^i\phi & \cos\phi\geq 0 \\ R_0+R_0\sum_{i=2,3} b_i\cos^i\phi & \cos\phi<0 \end{cases}. \tag{S6}$$

Here R_0 is the size parameter, and $a(b)_{2,3}$ are optimized as $a_2=-0.1329$, $a_3=0.0948$, $b_2=-0.0642$, and $b_3=-0.0224$.

The emission and coupling properties of the deformed microcavity can be well described by ray dynamics and tunneling processes. The features of the internal ray dynamics are typically presented in the Poincaré surface of section (SOS) (*26*), whose ordinate characterizes approximately the magnitude of the angular momentum of photons. The SOS of the cavity with the boundary defined by Eq. S6 for counter-clockwise (CCW) modes is shown in **Fig. S6B**, with coordinates defined in **Fig. S6A**. In SOS, the ray dynamics is mostly chaotic (black points), except for some regular orbits (red curves), including both islands and Kolmogorov–Arnold–Moser (KAM) curves. Ray dynamically, these three different structures are disjoint in SOS. However, in wave optics, dynamic tunneling between the regular orbits and neighboring chaotic orbits can take place (*25, 29-31, 43-46*), where the latter eventually refract out from the cavity following an unstable manifolds channel (green curves) (*44*) when crossing the total internal reflection critical line (red dashed line). It is worth noting that the chaotic motion along the unstable manifolds channel is a momentum transformation process. As a result, a universal directional emission pattern can be expected by properly designing an unstable manifolds channel (*43, 44*). The far-field emission patterns of the deformed microcavity from ray and wave simulations are shown in **Figs. S7A** and **S7B**, respectively. The primary emission is along the 180^o far-field direction, showing an excellent ray-wave correspondence. For all the experiments and simulations in this paper, the tapered fiber waveguide is placed at the primary emission position of the cavity with $\phi=\pi/2$ or $3\pi/2$, while the incident light entered the cavity along the direction inverse to the primary emission (as shown in **Fig. S6A**). In addition, the directional emission can also be designed by transformation optics (*47*).

On the other hand, benefiting from the principle of reversibility, the nanowaveguide field can also couple with WGMs by entering the stable manifolds of unstable periodic orbits (*44*) and subsequent dynamic tunneling. Note that the stable manifolds of the different periodic orbits are almost parallel in the leaky region in SOS (*48*). **Figure S8** shows two pathways formed by subsequent 50 bounces, along which the incident rays can reach the chaotic areas near the lowest KAM curve in a very short time. Red curves represent stable manifolds of the unstable period-4 (**Fig. S8A**)/period-5 (**Fig. S8B**) orbit. The initial incident rays (within the coupling region shown by the black dashed ellipse) locate under the critical line around $\phi = 3\pi/2$. In **Fig. S8A**, rays converge to the unstable period-4 orbit through stable manifolds and then escape from unstable manifolds. Consequently, they quickly approach the KAM curve, where chaotic rays more likely tunnel to the regular whispering-gallery region. To avoid confusion, rays which cross the critical line after 10 bounces are not plotted here. Likewise, rays entering the coupling region may also evolve along the stable manifolds of the unstable period-5 orbit as shown in **Fig. S8B**, therefore they reach a larger angular momentum rapidly, and from there it can tunnel to the WGM region. It is noted that the unstable period-4 orbit is closer to the critical line than that the unstable period-5 orbit. Thus, fewer rays reach the higher angular momentum region in **Fig. S8A** compared with **Fig. S8B**. The whole dynamic process is free from momentum conservation, i.e., the broadband coupling can be achieved assisted by the chaotic motion and dynamic tunneling.

B. Dispersion engineering of a fiber waveguide

Dispersions of fiber waveguides with diameters of 0.5 μm and 1.5 μm are presented in **Fig. S9** as blue curves, where both material and geometric dispersions have been taken into account. To compare effective indices (propagating constants) between the cavity mode and the fiber guided mode, we transform the effective refractive index of the fiber waveguide to the cavity polar coordinate as following, $n_{w,eff} \sim n_w/[1+\delta/3+2\delta^2/15]$ with $\delta = -\rho/R_0$, where R_0 is the cavity principal radius, and ρ is the distance between the cavity boundary and the center of the fiber waveguide (*14, 49, 50*).

Given the effective penetration depth of evanescent field, the fiber-cavity gap varies within a wavelength range, i.e., $0 \le \text{gap} \le \lambda$, which causes the broadening of the curves. In addition, the effective indices of fundamental WGMs with different wavelengths are also shown as the dashed red curve in **Fig. S9**. The principal and minor diameters of the microtoroid here are 60 μm and 4 μm, respectively. Note that there is no intersection point between dispersion curves of 0.5 μm fiber and WGMs, representing that fiber modes field only couple with WGMs indirectly through the chaotic dynamics instead of direct phase-matched coupling in this case.

III. Additional 3D FDTD Numerical Simulations

A. Comparison of the chaotic deformed cavity and a non-chaotic ellipse cavity

To clarify the role of chaotic dynamics in the momentum-transformed excitation process, we have performed comparative 3D FDTD simulations by using an elliptical microdisk resonator. It should be noted that the SOS of an ellipse resonator consists of invariant curves and islands. In other words, there is no chaos in the SOS of an ellipse resonator.

In detail, we use an elliptical microdisk as the counterpart. The diameter and deformation (relative difference in maximum and minimum diameters) of the ellipse cavity is the same as the deformed cavity used in this paper. In the simulation, electrical dipoles in TE polarization are randomly placed inside the cavities to excite WGMs of both resonators (**Fig. S10A**). Fundamental WGMs exist in both deformed cavity (**Fig. S10B**) and the ellipse cavity (**Fig. S10C**) by recording the in-cavity energy. On the other hand, the transmission spectra can also be obtained from frequency domain monitors in the simulation by externally exciting the same modes using a 0.5-μm-diameter fiber waveguide (**Fig. S10D**). The transmission spectra indicate that the coupling to the deformed cavity (**Fig. S10E**) is over 20 times higher than the ellipse cavity (**Fig. S10F**), showing an apparent evidence of the role of chaotic dynamics in the momentum-transformed excitation process. The very small excitation of the fundamental mode in the ellipse cavity can be attributed to the phase-matching (*51*) or scattering (*23*) excitation. It should be noted that the linewidths (i.e., Q factors) of the fundamental modes here are dominated by the artificial absorption of materials, which is added to make the simulations computationally affordable.

B. Transient energy decay of the momentum-transformed coupling process

The transient total field energies inside the microresonator and their decay rates during the momentum-transformed coupling process are extracted from the short time frequency domain monitors in 3D FDTD simulation, which are shown as the black and red curves in **Fig. S11**, respectively. The energy decay of the microresonator shows a single exponential decay after 50 ps when the WGM is being established, and the decay rate (50 GHz) is in agreement with the resonant linewidth (~45 GHz) (i.e., Q factor) reading from the transmission spectrum, which is dominated by the artificial absorption of materials.

C. Coupling efficiency and Q factor versus the microresonator deformation

There is a trade-off between the Q factor and the coupling efficiency of WGMs in a deformed microresonator. A larger deformation typically leads to a higher coupling efficiency, but a smaller Q factor. **Figure S12** shows the simulated coupling efficiency and Q factors, derived from the transmission spectra, depending on deformations. The deformation here is defined as the relative difference in largest and smallest diameter of the resonator. The variation of deformation is achieved by changing the shape coefficients proportionally. We select the deformation of 4% as a trade-off between the Q factor and the coupling efficiency in this paper.

D. Transient dynamics in the monochromatic case

We have also run a 3D FDTD control simulation of coupling to the same mode as in **Fig. S13** in the monochromatic case, i.e., using a much longer pulse (500 ps in duration time). This simulation is approaching the monochromatic limiting case because the pulse duration is much longer than the WGM decay time (~ 10 ps). As shown in **Fig. S13**, the results are similar with that of the short pulse case in **Fig. S1**. One difference between short and long pulse excitations is that the final stable field profile (after 100 ps) of long pulse excitation (**Fig. S13**) is a hybrid among WGM, chaotic modes, and external guided field, because the pulse duration is longer than the simulation time. While the final stable

field profile (200 ps) of the short pulse case (**Fig. S1**) is nearly a pure WGM, similar with mode profile in Ref. (*52*). Consequently, we choose the short pulse excitation to analyze the transient dynamic process and transmission spectra.

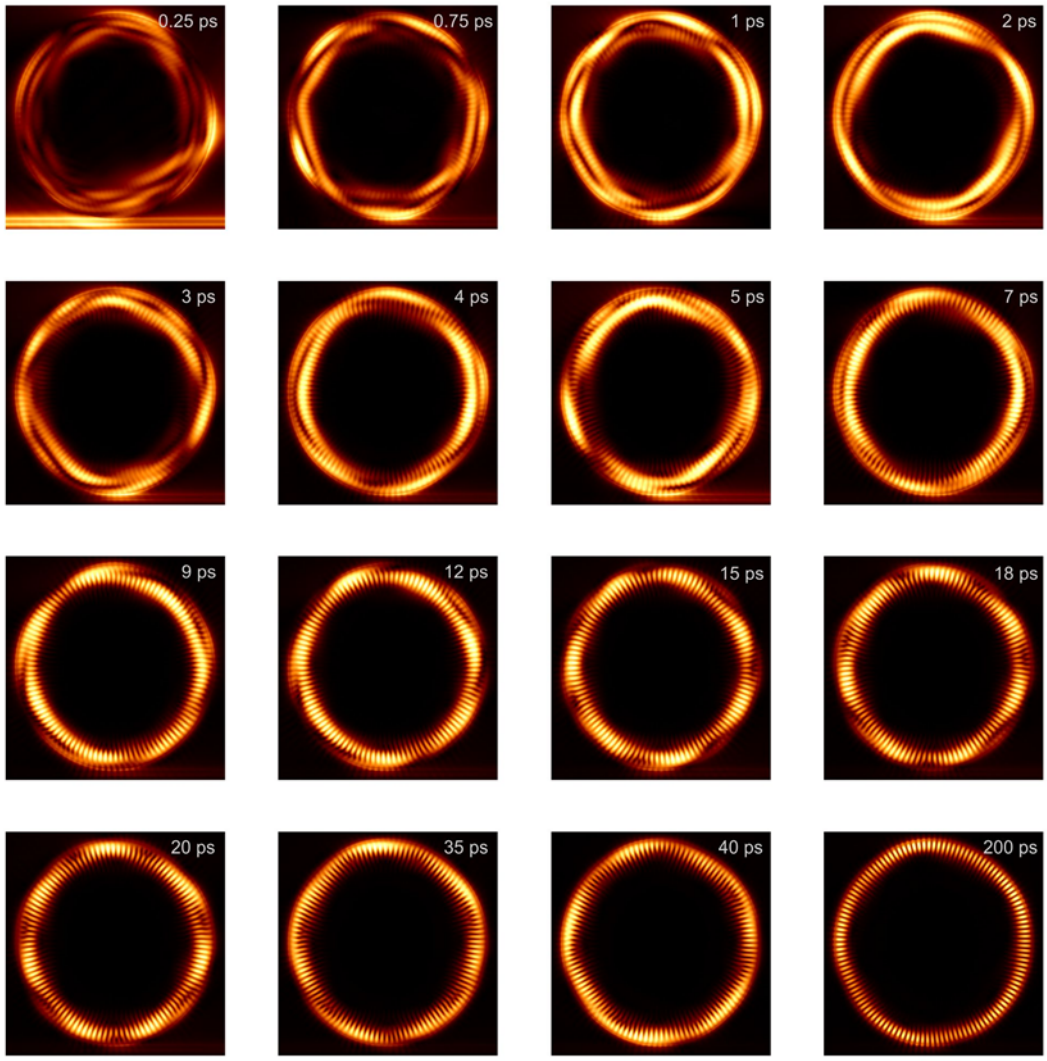

Fig. S1

Snapshots of spatial intensity distribution with a pulse duration of 10 fs in 3D FDTD simulations, showing the momentum transformation process and coupling to a WGM. The fields are normalized individually.

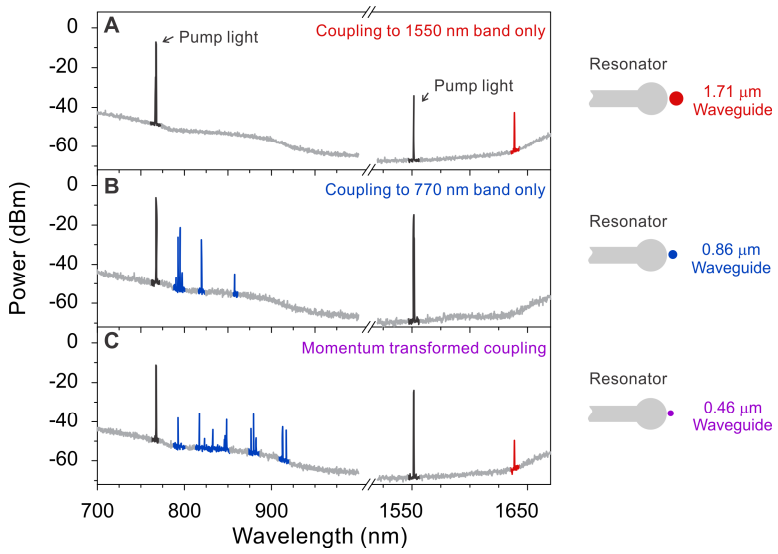

Fig. S2

Broadband Raman lasing in a deformed microresonator. The microresonator is pumped at both 768 nm and 1,551 nm. **A**, **B**, The Raman lasing is only observed in the phase-matched band. The waveguide with 1.71-μm-diameter phase matches to 1,550 nm band and the 0.86-μm-diameter waveguide phase matches to 770 nm band. **C**, Co-excitation of Raman lasing at 768 nm and 1,551 nm is observed using the chaos-assisted scheme. A 0.46-μm-diameter waveguide is used to excite chaotic fields and enable the broadband coupling.

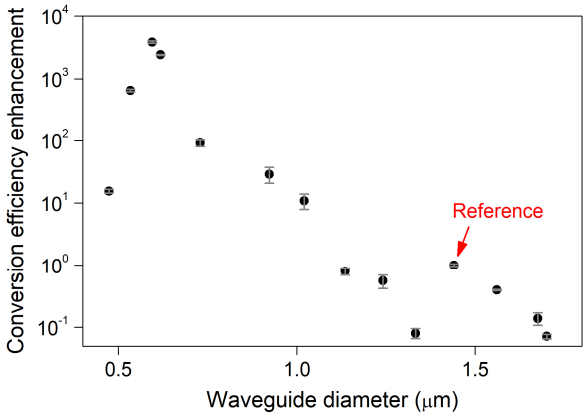

Fig. S3

The enhancement of conversion efficiency for third-harmonic generation versus diameters of the tapered fiber waveguide. The conversion efficiency is normalized to the highest conversion efficiency of direct phase-matched coupling using a micro-sized tapered fiber waveguide (reference is marked by red arrow).

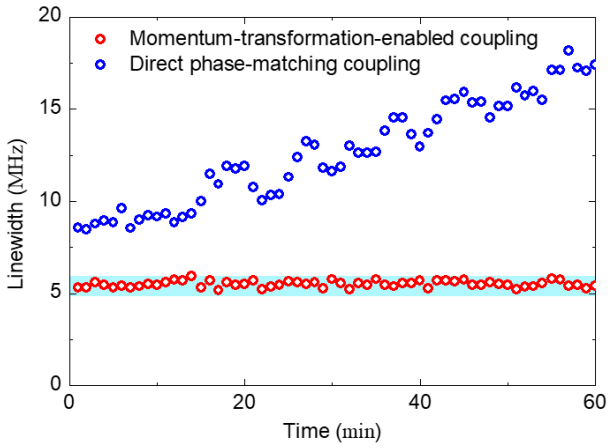

Fig. S4

Time stability of the linewidths for the same asymmetric cavity mode coupled with both 0.46-μm fiber (red) and 1.71-μm fiber (blue).

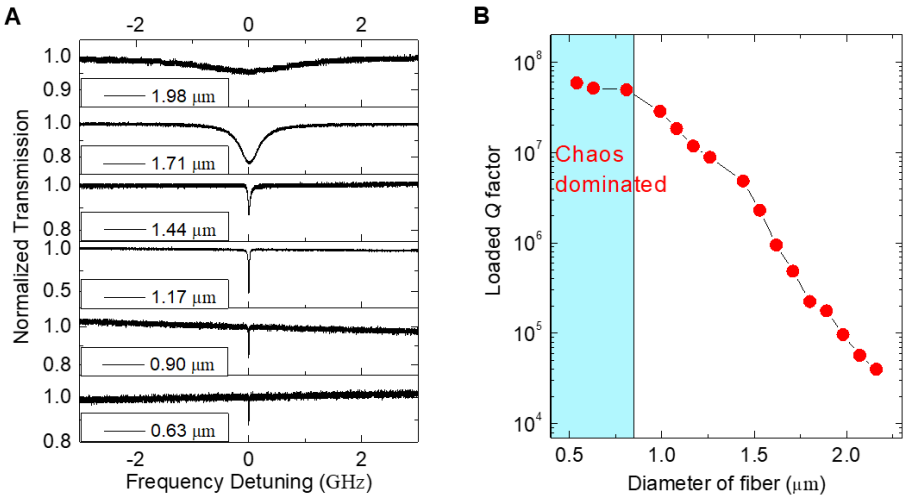

Fig. S5

A, Transmission spectra of different-sized fibers contacted to the equatorial plane of a high-Q toroid. **B**, Loaded Q factors of an asymmetric cavity mode with the contact coupling using different-sized fibers.

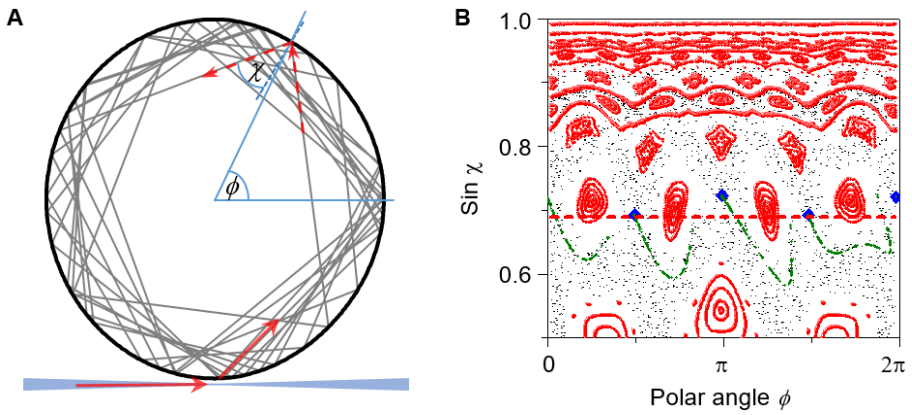

Fig. S6

A, Sketch of a deformed microcavity coupled to an optical fiber waveguide. The gray trajectories plot the subsequent 50 bounces after the first ray is coupled into the cavity. **B**, Poincaré SOS for the internal ray dynamics with the Birkhoff coordinates $\sin\chi$ and ϕ, where χ denotes the incident angle and ϕ the angular position of the reflection point, also defined in **A**. Black discrete points: chaotic trajectories; red curves: periodic and quasi-periodic orbits; red dashed line: critical line $\sin\chi=1/n_s$, with n_s the refractive index of silica; green curves: unstable manifolds of the unstable period-4 orbit (blue diamonds).

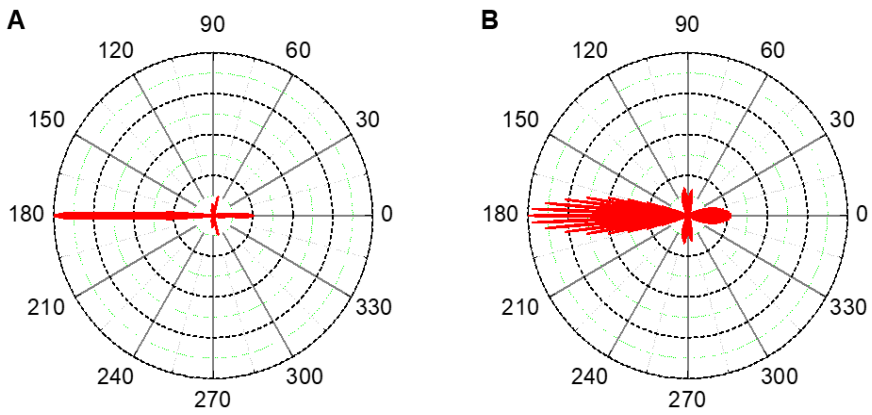

Fig. S7

Far-field emission patterns for a TM fundamental mode with $kR_0 \sim 72$ from ray (**A**) and wave (**B**) simulations, respectively.

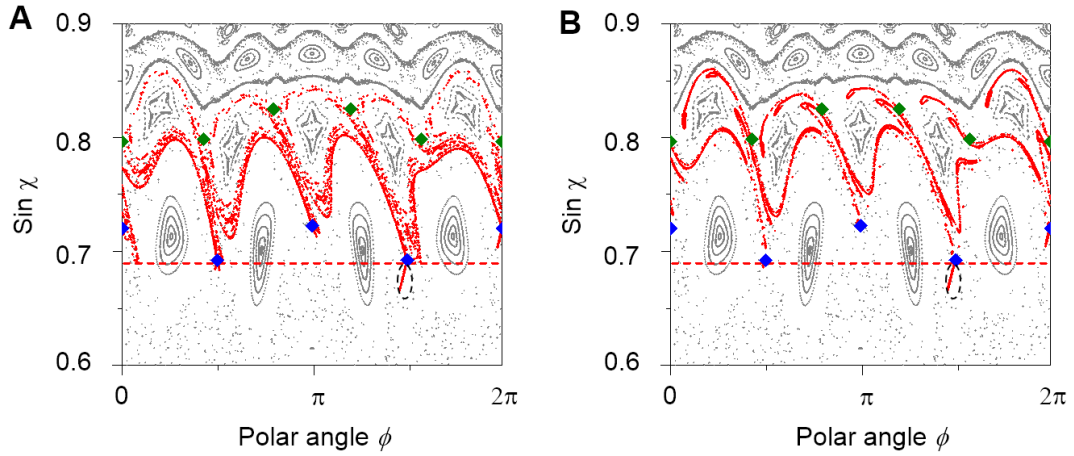

Fig. S8

A, Stable manifolds (red curves) of the unstable period-4 orbit (blue diamonds). **B**, Stable manifolds (red curves) of the unstable period-5 orbit (green diamonds). Black dashed ellipse: coupling region.

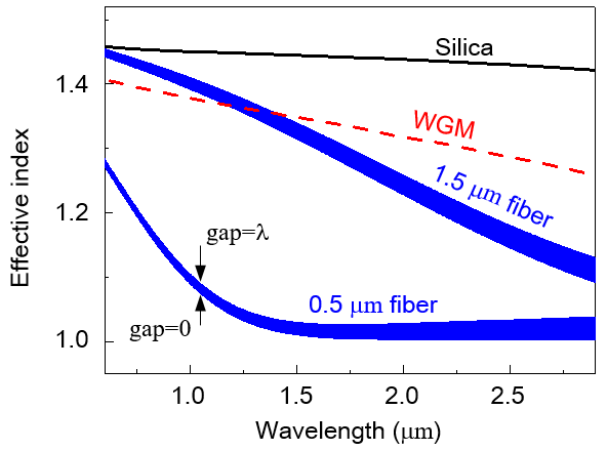

Fig. S9

Effective indices of bulk silica (black solid curve), cavity modes (red dashed curve), and fiber waveguide modes with a variable fiber-cavity gap ($0 \le \text{gap} \le \lambda$) for different fiber diameters *d* (blue broadened curves).

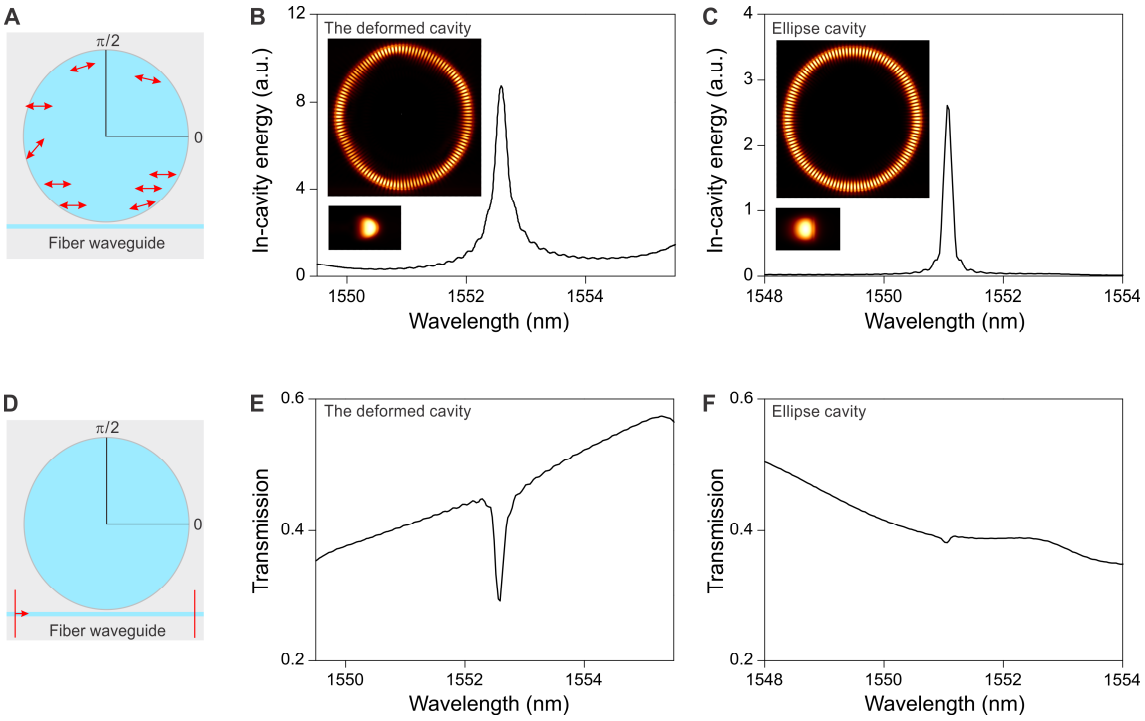

Fig. S10

Comparison of the chaotic deformed cavity and a non-chaotic ellipse cavity. **A**, Electrical dipoles are randomly placed in a chaotic deformed cavity and a non-chaotic ellipse cavity to excite the fundamental TE modes. **B**, **C**, The excited in-cavity energy spectra of the deformed cavity and the ellipse cavity, respectively. **D**, Externally exciting the same TE modes through a fiber waveguide with a diameter of 0.5 μm. **E**, **F**, Transmission spectra of the deformed cavity and the ellipse cavity with fiber waveguide excitation, respectively. The corresponding mode profiles of the fundamental TE modes are shown in the insets of **B** and **C**.

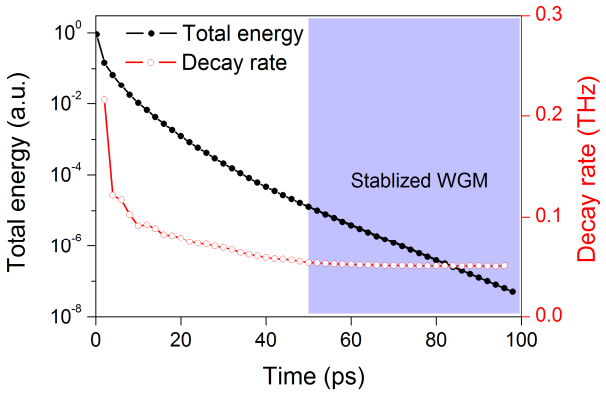

Fig. S11

Transient total field energy and decay rate of the momentum-transformation-enabled coupling process shown in Fig. 2 in the main text.

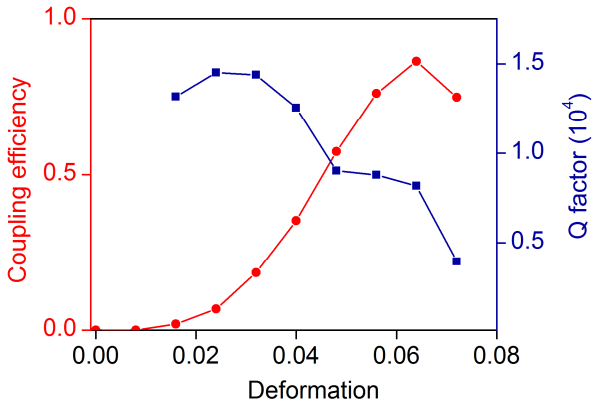

Fig. S12

Numerical simulation results of coupling efficiencies and *Q* factors on the microresonator deformation. The deformation is defined as the relative difference in largest and smallest diameter of the resonator. In the numerical simulation, the *Q* factors are deliberately lowered by artificial absorption to have simulations computationally affordable.

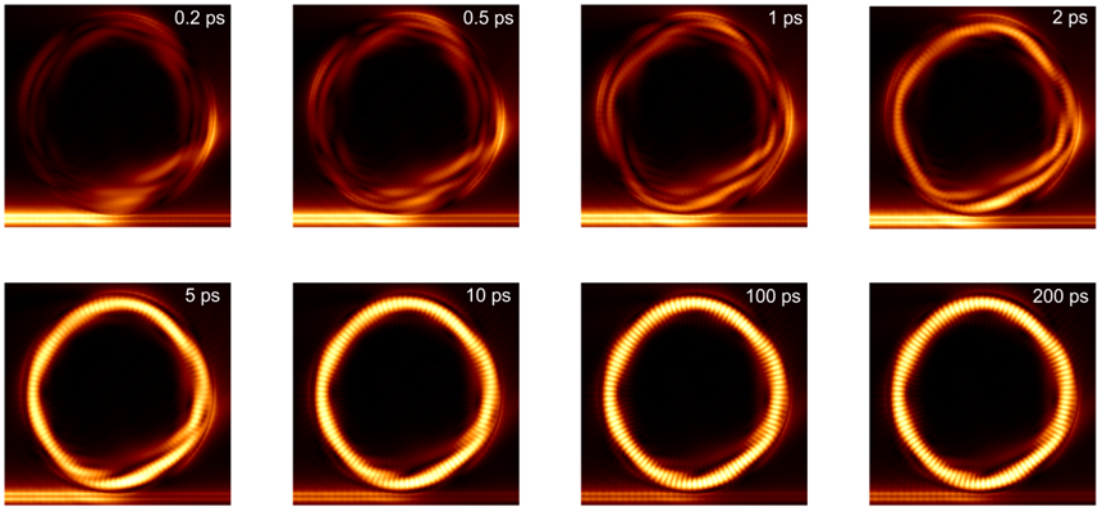

Fig. S13

Snapshots of transient dynamics of the momentum-transformation-enabled efficient coupling excited by a 500-ps long pulse. From the beginning to 2 ps, the light is being refracted into chaotic modes of microresonator from a 0.5-μm-diameter nanowaveguide. Snapshots of 2 ps and 5 ps show the light coupling into a WGM. Snapshots of 100 ps and 200 ps show the stabilized hybrid among the WGM, the chaotic modes, and the external guided field.

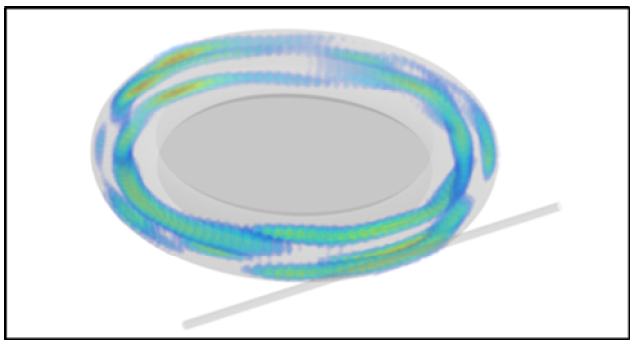

Movie S1

3D simulation illustrating the dynamics of chaos-assisted momentum-transformation-enabled coupling. The light from the tapered fiber is refracted into the cavity, followed by chaotic motion in the deformed cavity. Finally, the light is coupled into a high finesse WGM. The intensity of optical electrical fields from 0 to 200 ps are shown in the movie. The field is normalized to individual frames. The time scale bar indicates the simulation time. The sampling rate for 0 to 20 ps is 0.1 ps per frame, for 20 ps to 200 ps is 1 ps per frame.

Technical notes: VLC media player is recommended to play this supplementary movie, which is an open source software available at http://www.videolan.org/

References and Notes

1. A. Imamoğlu, H. Schmidt, G. Woods, M. Deutsch, Strongly interacting photons in a nonlinear cavity. *Phys. Rev. Lett.* **79**, 1467–1470 (1997). doi:10.1103/PhysRevLett.79.1467

2. T. Carmon, K. J. Vahala, Visible continuous emission from a silica microphotonic device by third-harmonic generation. *Nat. Phys.* **3**, 430–435 (2007). doi:10.1038/nphys601

3. R. W. Andrews, R. W. Peterson, T. P. Purdy, K. Cicak, R. W. Simmonds, C. A. Regal, K. W. Lehnert, Bidirectional and efficient conversion between microwave and optical light. *Nat. Phys.* **10**, 321–326 (2014). doi:10.1038/nphys2911

4. A. Rueda, F. Sedlmeir, M. C. Collodo, U. Vogl, B. Stiller, G. Schunk, D. V. Strekalov, C. Marquardt, J. M. Fink, O. Painter, G. Leuchs, H. G. L. Schwefel, Efficient microwave to optical photon conversion: An electro-optical realization. *Optica* **3**, 597 (2016). doi:10.1364/OPTICA.3.000597

5. C. Dong, V. Fiore, M. C. Kuzyk, H. Wang, Optomechanical dark mode. *Science* **338**, 1609–1613 (2012). doi:10.1126/science.1228370 Medline

6. J. T. Hill, A. H. Safavi-Naeini, J. Chan, O. Painter, Coherent optical wavelength conversion via cavity optomechanics. *Nat. Commun.* **3**, 1196 (2012). doi:10.1038/ncomms2201 Medline

7. T. J. Kippenberg, R. Holzwarth, S. A. Diddams, Microresonator-based optical frequency combs. *Science* **332**, 555–559 (2011). doi:10.1126/science.1193968 Medline

8. T. Herr, V. Brasch, J. D. Jost, C. Y. Wang, N. M. Kondratiev, M. L. Gorodetsky, T. J. Kippenberg, Temporal solitons in optical microresonators. *Nat. Photonics* **8**, 145–152 (2014). doi:10.1038/nphoton.2013.343

9. N. Yu, P. Genevet, M. A. Kats, F. Aieta, J.-P. Tetienne, F. Capasso, Z. Gaburro, Light propagation with phase discontinuities: Generalized laws of reflection and refraction. *Science* **334**, 333–337 (2011). doi:10.1126/science.1210713 Medline

10. C. Monroe, J. Kim, Scaling the ion trap quantum processor. *Science* **339**, 1164–1169 (2013). doi:10.1126/science.1231298 Medline

11. K. J. Vahala, Optical microcavities. *Nature* **424**, 839–846 (2003). doi:10.1038/nature01939 Medline

12. V. Sandoghdar, F. Treussart, J. Hare, V. Lefèvre-Seguin, J. Raimond, S. Haroche, Very low threshold whispering-gallery-mode microsphere laser. *Phys. Rev. A* **54**, R1777–R1780 (1996). doi:10.1103/PhysRevA.54.R1777 Medline

13. A. Mazzei, S. Götzinger, L. S. Menezes, V. Sandoghdar, O. Benson, Optimization of prism coupling to high-Q modes in a microsphere resonator using a near-field probe. *Opt. Commun.* **250**, 428–433 (2005). doi:10.1016/j.optcom.2005.02.054

14. D. R. Rowland, J. D. Love, Evanescent-wave coupling of whispering-gallery modes of a dielectric cylinder. *IEE Proc. J Optoelectron.* **140**, 177–188 (1993). doi:10.1049/ip-j.1993.0028

15. J. C. Knight, G. Cheung, F. Jacques, T. A. Birks, Phase-matched excitation of whispering-gallery-mode resonances by a fiber taper. *Opt. Lett.* **22**, 1129–1131 (1997). doi:10.1364/OL.22.001129 Medline

16. M. Cai, O. Painter, K. J. Vahala, Observation of critical coupling in a fiber taper to a silica-microsphere whispering-gallery mode system. *Phys. Rev. Lett.* **85**, 74–77 (2000). doi:10.1103/PhysRevLett.85.74 Medline

17. A. Yariv, Critical coupling and its control in optical waveguide-ring resonator systems. *IEEE Photonics Technol. Lett.* **14**, 483–485 (2002). doi:10.1109/68.992585

18. T. Carmon, S. Y. Wang, E. P. Ostby, K. J. Vahala, Wavelength-independent coupler from fiber to an on-chip cavity, demonstrated over an 850nm span. *Opt. Express* **15**, 7677–7681 (2007). doi:10.1364/OE.15.007677 Medline

19. K. Srinivasan, O. Painter, Linear and nonlinear optical spectroscopy of a strongly coupled microdisk-quantum dot system. *Nature* **450**, 862–865 (2007). doi:10.1038/nature06274 Medline

20. D. C. Aveline, L. M. Baumgartel, G. Lin, N. Yu, Whispering gallery mode resonators augmented with engraved diffraction gratings. *Opt. Lett.* **38**, 284–286 (2013). doi:10.1364/OL.38.000284 Medline

21. V. Ilchenko, A. Savchenkov, L. Maleki, U.S. Patent 7929589 (2011).

22. Q. J. Wang, C. Yan, N. Yu, J. Unterhinninghofen, J. Wiersig, C. Pflügl, L. Diehl, T. Edamura, M. Yamanishi, H. Kan, F. Capasso, Whispering-gallery mode resonators for highly unidirectional laser action. *Proc. Natl. Acad. Sci. U.S.A.* **107**, 22407–22412 (2010). doi:10.1073/pnas.1015386107 Medline

23. Y. C. Liu, Y.-F. Xiao, X.-F. Jiang, B.-B. Li, Y. Li, Q. Gong, Cavity-QED treatment of scattering-induced free-space excitation and collection in high-Q whispering-gallery microcavities. *Phys. Rev. A* **85**, 013843 (2012). doi:10.1103/PhysRevA.85.0138..43

24. J. Zhu, Ş. K. Özdemir, H. Yilmaz, B. Peng, M. Dong, M. Tomes, T. Carmon, L. Yang, Interfacing whispering-gallery microresonators and free space light with cavity enhanced Rayleigh scattering. *Sci. Rep.* **4**, 6396 (2014). doi:10.1038/srep06396 Medline

25. H. Cao, J. Wiersig, Dielectric microcavities: Model systems for wave chaos and non-Hermitian physics. *Rev. Mod. Phys.* **87**, 61–111 (2015). doi:10.1103/RevModPhys.87.61

26. J. U. Nöckel, A. D. Stone, Ray and wave chaos in asymmetric resonant optical cavities. *Nature* **385**, 45–47 (1997). doi:10.1038/385045a0

27. C. Gmachl, F. Capasso, E. E. Narimanov, J. U. Nockel, A. D. Stone, J. Faist, D. L. Sivco, A. Y. Cho, High-power directional emission from microlasers with chaotic resonators. *Science* **280**, 1556–1564 (1998). doi:10.1126/science.280.5369.1556 Medline

28. S. Lacey, H. Wang, D. H. Foster, J. U. Nöckel, Directional tunneling escape from nearly spherical optical resonators. *Phys. Rev. Lett.* **91**, 033902 (2003). doi:10.1103/PhysRevLett.91.033902 Medline

29. J. Yang, S.-B. Lee, S. Moon, S.-Y. Lee, S. W. Kim, T. T. A. Dao, J.-H. Lee, K. An, Pump-induced dynamical tunneling in a deformed microcavity laser. *Phys. Rev. Lett.* **104**, 243601 (2010). doi:10.1103/PhysRevLett.104.243601 Medline

30. S. Shinohara, T. Harayama, T. Fukushima, M. Hentschel, T. Sasaki, E. E. Narimanov, Chaos-assisted directional light emission from microcavity lasers. *Phys. Rev. Lett.* **104**, 163902 (2010). doi:10.1103/PhysRevLett.104.163902 Medline

31. Q. Song, L. Ge, B. Redding, H. Cao, Channeling chaotic rays into waveguides for efficient collection of microcavity emission. *Phys. Rev. Lett.* **108**, 243902 (2012). doi:10.1103/PhysRevLett.108.243902 Medline

32. Materials and methods are available as supplementary materials.

33. X.-F. Jiang, Y. F. Xiao, C. L. Zou, L. He, C. H. Dong, B. B. Li, Y. Li, F. W. Sun, L. Yang, Q. Gong, Highly unidirectional emission and ultralow-threshold lasing from on-chip ultrahigh-Q microcavities. *Adv. Mater.* **24**, OP260–OP264 (2012). doi:10.1002/adma.201201229 Medline

34. Lumerical Solutions, Inc., www.lumerical.com/tcad-products/fdtd/.

35. Q.-F. Yang, X.-F. Jiang, Y.-L. Cui, L. Shao, Y.-F. Xiao, Dynamical tunneling-assisted coupling of high-Q deformed microcavities using a free-space beam. *Phys. Rev. A* **88**, 023810 (2013). doi:10.1103/PhysRevA.88.023810

36. S. M. Spillane, T. J. Kippenberg, K. J. Vahala, Ultralow-threshold Raman laser using a spherical dielectric microcavity. *Nature* **415**, 621–623 (2002). doi:10.1038/415621a Medline

37. B. Min, T. J. Kippenberg, K. J. Vahala, Compact, fiber-compatible, cascaded Raman laser. *Opt. Lett.* **28**, 1507–1509 (2003). doi:10.1364/OL.28.001507 Medline

38. F. Bo, S. H. Huang, Ş. K. Özdemir, G. Zhang, J. Xu, L. Yang, Inverted-wedge silica resonators for controlled and stable coupling. *Opt. Lett.* **39**, 1841–1844 (2014). doi:10.1364/OL.39.001841 Medline

39. Y.-Z. Yan, C.-L. Zou, S.-B. Yan, F.-W. Sun, Z. Ji, J. Liu, Y.-G. Zhang, L. Wang, C.-Y. Xue, W.-D. Zhang, Z.-F. Han, J.-J. Xiong, Packaged silica microsphere-taper coupling system for robust thermal sensing application. *Opt. Express* **19**, 5753–5759 (2011). doi:10.1364/OE.19.005753 Medline

40. F. Monifi, S. K. Özdemir, J. Friedlein, L. Yang, Encapsulation of a fiber taper coupled microtoroid resonator in a polymer matrix. *IEEE Photonics Technol. Lett.* **25**, 1458–1461 (2013). doi:10.1109/LPT.2013.2266573

41. Y.-D. Yang, S.-J. Wang, Y.-Z. Huang, Investigation of mode coupling in a microdisk resonator for realizing directional emission. *Opt. Express* **17**, 23010–23015 (2009). doi:10.1364/OE.17.023010 Medline

42. L. Shao, X.-F. Jiang, X.-C. Yu, B.-B. Li, W. R. Clements, F. Vollmer, W. Wang, Y.-F. Xiao, Q. Gong, Detection of single nanoparticles and lentiviruses using microcavity resonance broadening. *Adv. Mater.* **25**, 5616–5620 (2013). doi:10.1002/adma201302572 Medline

43. C.-L. Zou, F.-W. Sun, C.-H. Dong, F.-J. Shu, X.-W. Wu, J.-M. Cui, Y. Yang, Z.-F. Han, G.-C. Guo, High-Q and unidirectional emission whispering gallery modes: Principles and design. *IEEE J. Sel. Top. Quantum Electron.* **19**, 1–6 (2013). doi:10.1109/JSTQE.2012.2220896

44. J. Wiersig, M. Hentschel, Combining directional light output and ultralow loss in deformed microdisks. *Phys. Rev. Lett.* **100**, 033901 (2008). doi:10.1103/PhysRevLett.100.033901 Medline

45. Y.-F. Xiao, X.-F. Jiang, Q.-F. Yang, L. Wang, K. Shi, Y. Li, Q. Gong, Tunneling-induced transparency in a chaotic microcavity. *Laser Photonics Rev.* **7**, L51–L54 (2013). doi:10.1002/lpor.201300042

46. J. Yang, S.-B. Lee, J.-B. Shim, S. Moon, S.-Y. Lee, S. W. Kim, J.-H. Lee, K. An, Enhanced nonresonant optical pumping based on turnstile transport in a chaotic microcavity laser. *Appl. Phys. Lett.* **93**, 061101 (2008). doi:10.1063/1.2968210

47. Y. Kim, S.-Y. Lee, J.-W. Ryu, I. Kim, J.-H. Han, H.-S. Tae, M. Choi, B. Min, Designing whispering gallery modes via transformation optics. *Nat. Photonics* **10**, 647–652 (2016). doi:10.1038/nphoton.2016.184

48. E. G. Altmann, Emission from dielectric cavities in terms of invariant sets of the chaotic ray dynamics. *Phys. Rev. A* **79**, 013830 (2009). doi:10.1103/PhysRevA.79.013830

49. Y.-F. Xiao, C.-L. Zou, B.-B. Li, Y. Li, C.-H. Dong, Z.-F. Han, Q. Gong, High-Q exterior whispering-gallery modes in a metal-coated microresonator. *Phys. Rev. Lett.* **105**, 153902 (2010). doi:10.1103/PhysRevLett.105.153902 Medline

50. B. Min, E. Ostby, V. Sorger, E. Ulin-Avila, L. Yang, X. Zhang, K. Vahala, High-Q surface-plasmon-polariton whispering-gallery microcavity. *Nature* **457**, 455–458 (2009). doi:10.1038/nature07627 Medline

51. C.-L. Zou, F.-J. Shu, F.-W. Sun, Z.-J. Gong, Z.-F. Han, G.-C. Guo, Theory of free space coupling to high-Q whispering gallery modes. *Opt. Express* **21**, 9982–9995 (2013). doi:10.1364/OE.21.009982 Medline

52. T. Carmon, H. G. L. Schwefel, L. Yang, M. Oxborrow, A. D. Stone, K. J. Vahala, Static envelope patterns in composite resonances generated by level crossing in optical toroidal microcavities. *Phys. Rev. Lett.* **100**, 103905 (2008). doi:10.1103/PhysRevLett.100.103905 Medline